



High-performance bifunctional oxygen electrocatalysts for zinc-air batteries over mesoporous Fe/Co-N-C nanofibers with embedding FeCo alloy nanoparticles

Congling Li, Mengchen Wu, Rui Liu*

Ministry of Education Key Laboratory of Advanced Civil Engineering Materials, School of Materials Science and Engineering and Institute for Advanced Study, Tongji University, 201804, Shanghai, China

ARTICLE INFO

Keywords:

Electrospinning
Hybrid nanofibers
FeCo alloy nanoparticles
Bifunctional electrocatalysts
Zn-Air battery

ABSTRACT

Mesoporous Fe/Co-N-C nanofibers with embedding FeCo nanoparticles (denote as FeCo@MNC) have been prepared from electrospun Fe/Co-N coordination compounds with bicomponent polymers consisting of polyvinylpyrrolidone (PVP) and polyacrylonitrile (PAN). The as-fabricated hybrid nanofibers exhibited one-dimensional mesoporous morphology, a large BET surface area and uniformly distributed active sites (e.g. FeCo alloy, Fe/Co-N). It elucidated that the co-existence of FeCo alloy and Fe/Co-N active sites could promote the catalytic activity of ORR and OER simultaneously. Essentially, the unique one-dimensional of nanofiber with observable porous morphology has indispensable contribution to charge transportation and exposure of active sites to O₂ adsorption when assembled into a rechargeable zinc-air battery. As a result, FeCo@MNC exhibited a low discharge-charge voltage gap (e.g. 0.9 V, discharge-charge at 20 mA cm⁻²), higher power density (e.g. 115 mW cm⁻², at 143 mA cm⁻²) and stability.

1. Introduction

The low cost, environmental friendliness, and high theoretical energy density have established Zn-air batteries as one of the most promising energy storage devices [1–3]. It is commonly acknowledged that oxygen evolution reaction (OER) and oxygen reduction reaction (ORR) play vital roles in charge and discharge processes for the rechargeable zinc-air batteries [4,5]. Albeit benchmark OER catalysts (e.g. IrO₂, RuO₂) and ORR catalysts (e.g. Pt/C) do possess high catalytic activity for accelerating the sluggish kinetics in respective fields, most commercial catalysts are associated with prohibitive costs and deterioration issues, and also it is to be regretted that they are unable to gratifyingly promote both reactions [6–8]. Therefore, it is a great but intriguing challenge to explore for alternative low-cost catalysts with high-efficiency activity that can be uploaded in a single cathode of scientific interest and economic value [9,10].

To maximize both ORR and OER catalytic performance within all-in-one catalyst, reasonable design of the catalyst's electrochemical composition has been concerned to seek for electrocatalysts towards both reactions. For ORR, amount evidence has showed that the metal-nitrogen-carbon (M-N-C, M = Fe, Co) could decrease the binding energies of the surface-adsorbed *OOH and *OH species, thus boosting

electrocatalytic activities of ORR [11,12]. For example, Wang et al. have prepared Fe-N-C catalyst derived from carbonization of poly-iron-phthalocyanine, which exhibited higher catalytic activity compared to 20 wt. % Pt/C [13]. On the other hand, bimetallic alloys such as CoNi, FeNi, or FeCo have been accepted as extremely effective active sites for OER, which showed enhanced activity and stability compared to their single-element counterparts [14–16]. For example, Yang et al. have synthesized NiCo alloy catalyst decorated on carbon nanofibers, which exhibited specific potential comparable to RuO₂ at the current density of 10 mA cm⁻² and displayed desirable long-term stability during OER process [17].

It is seemingly expected to merge the M-N-C and metals alloy in an as-fabricated bifunctional hybrid catalyst possessing highly efficient ORR and OER performance [18]. Various strategies such as self-assembling [19], ball milling [20], impregnating [21], and gridding [22], have been used for the construction of hybrid catalyst. As a result, a series of alloy catalysts have been encapsulated in N-doped carbon, which exhibit high electrochemical performance [15,16]. A typical example is FeCo@NC core-shell nanospheres supported on graphene, which showed efficient bifunctional ORR and OER catalytic activity as well as Zn-air battery [20]. Electrospinning has been emerged as a useful technique to entangle different ingredients into one-dimensional

* Corresponding author.

E-mail address: ruiliu@tongji.edu.cn (R. Liu).

<https://doi.org/10.1016/j.apcatb.2018.11.039>

Received 16 July 2018; Received in revised form 24 October 2018; Accepted 14 November 2018

Available online 17 November 2018

0926-3373/© 2018 Elsevier B.V. All rights reserved.

(1D) fibrous nanomaterials with a large scale production capability [23–25]. Especially, the 1D carbon nanomaterials obtained from electrospinning with larger aspect ratio (lower diameter or larger length) have been demonstrated excellent electrical conductivity as well as accelerate O₂ and electrolyte diffusion for a variety of electrochemical processes [26]. Keeping a stimulus with that desirable consequences, herein, we employed the use of electrospinning and synthesized FeCo alloy NPs decorated on Fe/Co-N-C nanofibers (denoted as FeCo@MNC) for ORR and OER as well as further for Zn-air battery. In the electrospinning process, we used Fe and Co 2, 2-bipyridine chelates as active species precursors, and polymer PAN & PVP as carbon precursor & pore former. Followed by carbonization, the obtained FeCo@MNC exhibited high efficient and stable catalytic performance during ORR and OER process as well as in Zn-air battery.

2. Experimental section

2.1. Synthesis of FeCo@MNC

Typically, FeCl₃·6H₂O (0.11 g) and 2,2-bipyridine (0.125 g) were dissolved in dimethylformamide (DMF, 2.0 g) and stirred for 2 h to form Fe-N coordination compound; Co(NO₃)₂·6H₂O (0.12 g) and 2,2-bipyridine (0.125 g) were dissolved in DMF (2.0 g) and stirred for 2 h to form Co-N coordination compound. Then, polyvinylpyrrolidone (C₆H₉NO)_n, M.W. 1 300 000, 0.25 g) and polyacrylonitrile ((C₃H₃N)_n, M.W. 150 000, 0.25 g) were added in the mixture of above solution, and stirred vigorously at room temperature for about 20 h. In a typically electrospinning process, DC voltage of 13 kV was applied between a syringe and a collector with receiving distance of 12 cm and solution feeding rate of 10 μL min⁻¹. The obtained nanofibers were stabilized at 280 °C in air for 1 h followed by carbonization at 900 °C under N₂ atmosphere for 2 h. After calcination, the target products **FeCo@MNC** nanofibers were synthesized successfully.

For comparison, **FeCo@NC** nanofibers were prepared by adding none 2, 2-bipyridine in the synthesis process of FeCo@MNC. **NC NFs** were prepared by adding neither metal salt nor 2, 2-bipyridine in the synthesis process of FeCo@MNC. FeCo@MNC nanofibers with a small amount of alloy nanoparticles (denoted as **FeCo@MNC-S**) were prepared using the same procedure as that of FeCo@MNC, except the decreased addition of FeCl₃·6H₂O (0.07 g) and Co(NO₃)₂·6H₂O (0.08 g). Similarly, **FeNC** and **CoNC** nanofibers were prepared in the absence of Co(NO₃)₂·6H₂O and FeCl₃·6H₂O, respectively.

2.2. Material characterizations

Scanning electron microscopy (SEM) images were carried out using a Hitachi-S4800 scanning electron microscope (10 kV). X-ray diffraction (XRD) patterns were obtained on a D8 Advance powder X-ray diffractometer (Bruker, Germany). Raman spectroscopy was performed on a GX-PT-1500 (150) instrument with a 532 nm excitation laser at a power of around 1 mW. Nitrogen adsorption-desorption isotherms were performed on a Quadrachrome adsorption instrument (Autosorb-iQ3; Quantachrome, America) at 77 K. Brunauer-Emmett-Teller (BET) method and the Barrett-Joyner-Halenda (BJH) model were employed to calculate the specific surface area and pore size distribution. Transmission electron microscopy (TEM) images and high-resolution TEM (HRTEM) images were conducted on a JEM-2100 Electron microscope (JEOL, Japan) at an acceleration voltage of 200 kV. X-ray photoelectron spectroscopic (XPS) analysis was performed on a ESCALAB 250Xi operated at 120 W.

2.3. Electrochemical measurements

The electrochemical measurements were performed at room temperature by using a PGSTAT302 N (Autolab) electrochemical analyzer with a three-electrode cell system. A glassy carbon electrode (RDE,

0.1962 cm², Pine Instrument Co., USA) or rotating ring disc electrode (RRDE) (carbon disk with surface area of 0.2475 cm² surrounded by a Pt ring with a surface area of 0.1866 cm²) modified with FeCo@MNC served as the working electrode, whereas Ag/AgCl (3.5 M KCl) and Pt electrode were used as reference and counter electrode in the measurement, respectively.

For the preparation of working electrode, the catalyst inks were prepared by sonicating 10 mg FeCo@MNC or commercial Pt/C catalyst (Johnson Matthey, 20 wt. % Pt) in a mixture of 1.25 mL ethanol and 30 μL Nafion (5%) for 1 h. A desired amount of the suspension was deposited onto the polished glassy carbon electrode and dried under a N₂-flow.

The electrochemical studies were performed by using cyclic voltammetry (CV) and linear sweep voltammetry (LSV) techniques at room temperature. The ORR measurements were carried out in O₂-saturated 0.1 M KOH solution. The loadings of FeCo@MNC and Pt/C on the working electrode were 0.36 mg cm⁻² and 0.10 mg cm⁻² in O₂-saturated 0.1 M KOH, respectively. The CVs, LSV, and chronoamperometric measurements were carried out at a scan rate of 10 mV s⁻¹. All potentials in this study were reported against Ag/AgCl was converted against the reversible hydrogen electrode (RHE). The OER performance of the catalysts was estimated from LSV in 1 M KOH at a scan rate of 5 mV s⁻¹ with iR-corrected and the catalysts total loading is 0.36 mg cm⁻².

Tafel slopes were calculated according to the Tafel equation:

$$\eta = b \log(j) + a; \quad (1)$$

Where η , j and b were the over potential, measured current density, and Tafel slope, respectively.

Hydrogen peroxide yields and the electron transfer number (n) were calculated using the equations below:

$$n = \frac{4I_D}{I_D + I_{R/N}}; \quad (2)$$

$$\%HO_2^- = 200 \times \frac{I_{R/N}}{I_D + I_{R/N}}; \quad (3)$$

where I_D , I_R and N were the disk current, ring current and the ring collection efficiency of the Pt ring disk, respectively. In this measurement, $N = 0.37$.

Electrochemical impedance spectroscopy (EIS) measurements were tested by an electrochemical workstation (Autolab, PGSTAT302 N) with an AC amplitude applied of 5 mV and frequency from 0.1 to 1000 kHz.

2.4. Zn-air battery

The catalyst ink consisting of 10 mg FeCo@MNC was dispersed in a mixture of 1.25 mL ethanol and 30 μL Nafion (5%). Zn-air batteries were tested in laboratory-constructed electrochemical cells. For the primary cells, a carbon paper electrode (3.14 cm²) loaded with FeCo@MNC (10 mg) was used as cathode, Zn foil was used as anode while the electrolyte was 6 M KOH (containing 0.2 M Zn(CH₃COO)₂). All Zn-air batteries were evaluated under ambient conditions. The galvanostatic discharge-charge cyclings were carried out on the LAND CT2001 A battery system at room temperature.

3. Results and discussion

3.1. Synthesis, structure, and composition of materials

Fig. 1 illustrated the synthetic route for FeCo@MNC. In brief, Fe and Co 2, 2-bipyridine chelates, PAN and PVP polymers were co-electrospun to form FeCo-Polymers nanofibers. After carbonization, FeCo alloy nanoparticles decorated on mesoporous Fe/Co-N-C nanofibers were obtained (FeCo@MNC). For comparison, FeCo@NC nanofibers were synthesized using the same procedure in the absence of 2, 2-bipyridine. Another control experiment was carried out by the similar procedure to

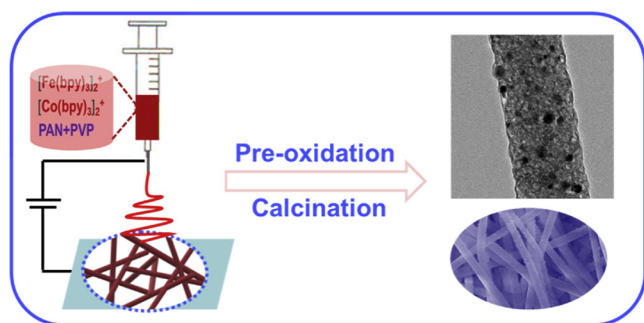


Fig. 1. Schematic synthesis process of FeCo alloy nanoparticles decorated mesoporous Fe/Co-N-C nanofibers.

obtain NC nanofibers by electrospinning PAN and PVP polymers only. It was noted that $\sim 400 \text{ cm}^2$ nanofiber film was obtained one hour per syringe in the current lab-setup electrospinning. Dai et al. achieved scalable manufacture of the pristine PI film through electrospinning by using solution continuously supplied syringe pump, 30 kV high-voltage power supply, and 0.80 mm (inner diameter) stainless steel gauge needle [24]. Therefore, electrospinning has demonstrated its large scale

of production ability

TEM images in Fig. 2a showed FeCo-Polymers nanofibers possessed a uniform fibrous structure with the diameter about 300 nm. After carbonization, the prepared FeCo@MNC nanofibers retained well-defined fibrous morphology with a diameter of about 200–300 nm with nanoparticles (NPs) decorated on the surface (SEM images in Fig. 2b). TEM images of FeCo@MNC in Fig. 2c showed observable porous structures of the nanofiber where bunches of nanoparticles decorated on the nanofibers. A 0.202 nm of distinct lattice fringe of NPs in HRTEM (Fig. 2d) was ascribed to the (110) crystalline facet of FeCo alloy, indicating the existence of FeCo structure in FeCo@MNC. Fig. 2e showed the STEM elements mapping results of FeCo@MNC, with C and N elements distributing homogeneously through the whole nanofibers. However, intriguingly to find that Fe and Co appeared not only inside the whole nanofibers but also on the surface of nanoparticles, implying the co-existence of both FeCo and Fe/Co-N-C structures in the nanofiber skeleton. As shown in XRD patterns (Fig. 3a), three characteristic diffraction peaks at around 44.8° , 65.3° and 82.7° in FeCo@MNC matched well with the (110), (200), (211) crystal facets of FeCo alloy (JCPDS No. 49-1518), according with the TEM results. A broad diffraction peak at 25° could be assigned to disordered graphitic (002) plane. Comparatively, FeCo@NC and NC nanofibers showed fibrous diameter of

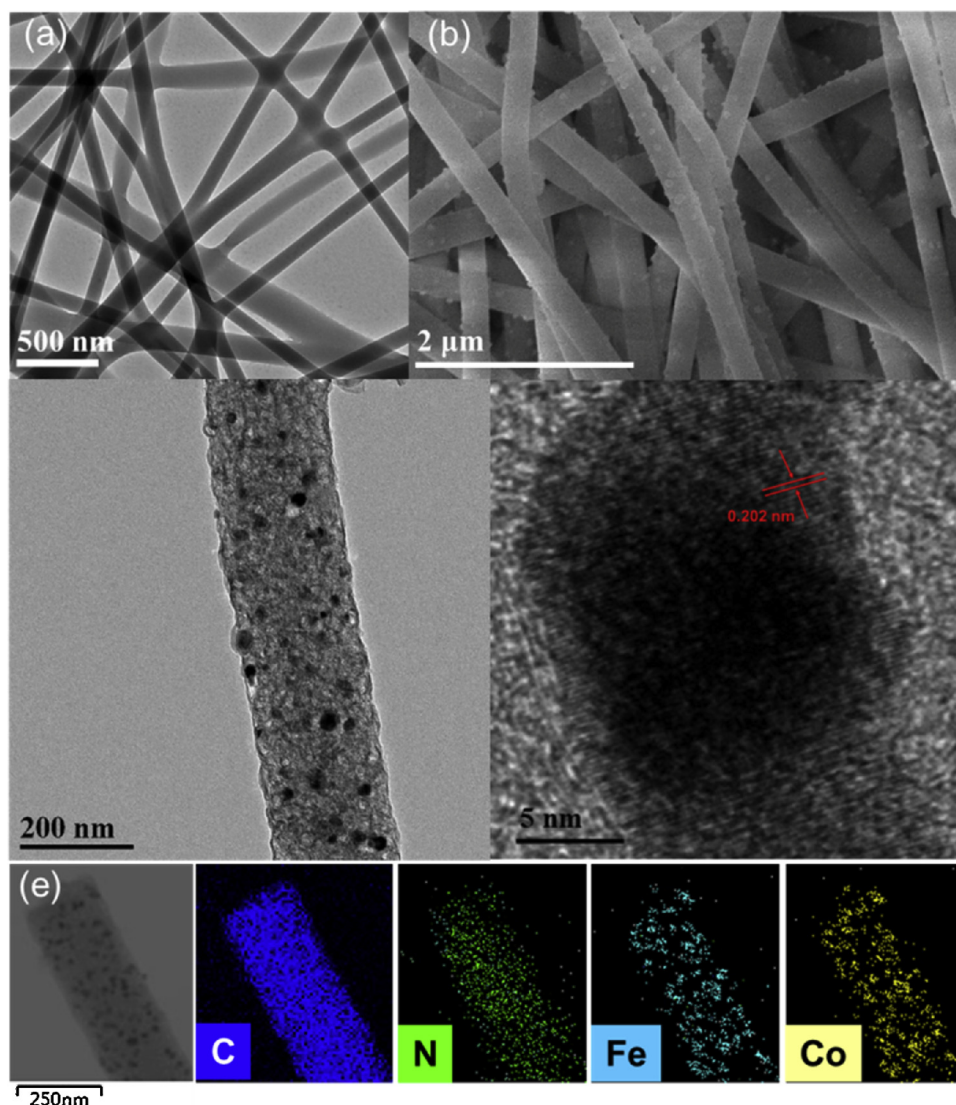


Fig. 2. (a) TEM images of FeCo-Polymers nanofibers. (b) SEM, (c) TEM images and (d) HRTEM images of FeCo@MNC. (e) HAADF-STEM image and the corresponding elemental mapping of FeCo@MNC.

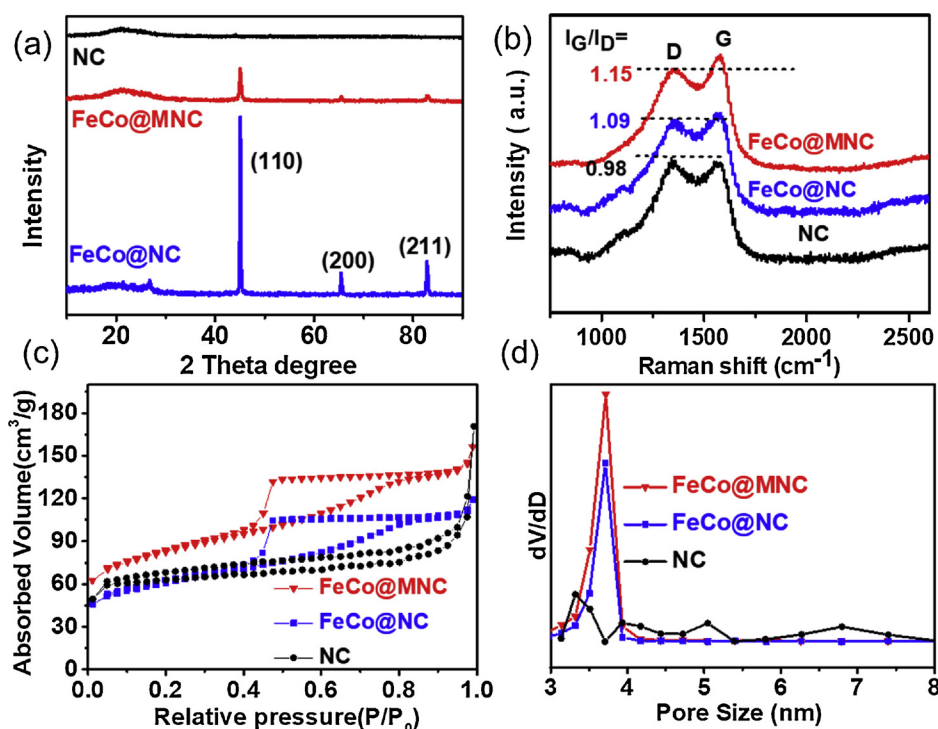


Fig. 3. (a) XRD patterns, (b) Raman spectra and (c) N₂ sorption isotherms and (d) The pore size distribution of the as-synthesized NC, FeCo@NC, and FeCo@MNC.

300–400 nm (Fig. S1a) and 200–300 nm (Fig. S1b), respectively. Besides, TEM images of NC (Fig. S2a) showed coarse surfaces and porous structures, while densely distributed FeCo nanoparticles could be seen in the case of FeCo@NC (Fig. S2b). The stronger XRD peak intensity of FeCo alloy in FeCo@NC compared to FeCo@MNC could be ascribed to the higher containing of FeCo alloy, which was in accordance with the TEM results. Only characteristic peak of graphitic was observed in the XRD of NC (Fig. 3a).

Raman spectra in Fig. 3b exhibited two distinct peaks around 1350 and 1580 cm⁻¹ in all three samples, corresponding to D and G band for carbon materials, respectively [27]. The value of I_G/I_D decreased in the following order: FeCo@MNC (1.15) > FeCo@NC (1.09) > NC (0.98), with a higher G/D ratio meaning a higher degree of graphitization contributing to high conductivity [28,29]. The specific surface area and pore characteristics of the prepared samples were measured by N₂ sorption isotherms (Fig. 3c). The H2 or H4 type hysteresis loops in the relative pressure range of 0.4–0.8 in the N₂ isotherms indicated the existence of the mesopores in FeCo@MNC, FeCo@NC and NC structures [30]. FeCo@MNC possessed the BET surface area of 345.3 m² g⁻¹, which was higher than FeCo@NC (263.5 m² g⁻¹) and NC (196.1 m² g⁻¹). The highest surface area of FeCo@MNC might be ascribed to their numerous ~ 4 nm sized pores (Fig. 3d) induced by decomposition of PVP and the 2, 2-bipyridine chelates in heat-treating process [31]. Otherwise, high degree of graphitization in FeCo@MNC also meant a sharp shrinking of carbon matrix and thus increased its porosity [32]. H4 type hysteresis loops and the smallest surface area of NC might be associated with lower degree of graphitization of non-metal supported carbon shrink in pyrolysis process [33].

XPS survey of FeCo@MNC (Fig. 4a) possessed the characteristic spectra of C1s (286.6 eV), N1s (400.2 eV), O1s (531.2 eV), Fe2p (709.5 eV) and Co2p (780.2 eV), confirming the successful doping of N, Fe and Co into the carbon [34]. The Fe2p spectra (Fig. 4b) showed Fe 2p_{3/2} (711.2 eV), Fe 2p_{1/2} (724.3 eV), and satellite peak (717.7 eV) suggesting the existence of Fe-N(C) species [35]. Similarly, Co2p spectra (Fig. 4c) showed Co 2p_{3/2} (780.6 eV), Co 2p_{1/2} (796.2 eV), and satellite peak (785.4 eV) suggesting the existence of Co-N(C) species [36]. Besides, the oxidized state of FeCo may be ascribed its

susceptibility to atmosphere [37]. Deconvoluted N1s peak (Fig. 4d) corresponding to pyridinic-N (398.2 eV), pyrrolic-N (400.0 eV), graphitic-N (401.1 eV) and pyridine N-O (404.3 eV) indicated a successful N-doping in the carbon matrix (N-C) [38]. For comparison, XPS survey of FeCo@NC were shown in Fig. S3, and the corresponding chemical composition were shown in Table S1. Combined with XPS (Table S1) and XRD (Fig. 3a) analysis, less N species containing and stronger peak intensity of FeCo alloy in FeCo@NC indicated fewer Fe/Co-N structure here compared with in FeCo@MNC. On the other hand, compared to FeCo@NC, N species in FeCo@MNC were obtained not only from PAN and PVP, but also from Fe and Co 2, 2-bipyridine chelates, which were more favourable to form Fe(Co)-(N)C moieties [39,40]. Besides, FeCo@MNC also possessed higher proportion of pyridinic-N structures. All these demanded structures distributed in FeCo@MNC should ascribe to its formation process: the metal Fe/Co ions first coordinate with 2, 2-bipyridine ligands to form Fe(Co)-N chelates, as electrospinning with polymers followed by carbonization, Fe(Co)-N and N-C structures were partly retained as well as the other part of them decomposed and developed into FeCo NPs dispersed within the carbon matrix.

3.2. Electrochemical characterization of catalysts

The electrocatalytic activities of the prepared materials for ORR were studied by CVs and linear sweep voltammetry (LSV) measurements in O₂-saturated 0.1 M KOH electrolyte. ORR peak potential E_p (Fig. 5a) and half-wave potential E_{1/2} (Fig. 5b) were observed for FeCo@MNC (E_p = 0.88 V; E_{1/2} = 0.86 V), FeCo@NC (E_p = 0.83 V; E_{1/2} = 0.81 V), and NC (E_p = 0.77 V; E_{1/2} = 0.75 V) in 0.1 M KOH. It was noted that the E_p and E_{1/2} of FeCo@MNC were higher than that of commercial Pt/C (E_p = 0.87 V; E_{1/2} = 0.85 V). In Fig. 5c, H₂O₂ yields for FeCo@MNC, FeCo@NC, NC and Pt/C were 6%, 10%, 16% and 4%, and the corresponding electron transfer number were 3.87, 3.81, 3.67 and 3.94, respectively, indicating a nearly four-electron pathway of FeCo@MNC during the ORR process. All the above indicated that FeCo@MNC possesses the best ORR electrocatalytic activity among the prepared catalysts. The electrocatalytic activity also could be evaluated from Tafel slope, as showed in Fig. 5d, FeCo@MNC displayed the

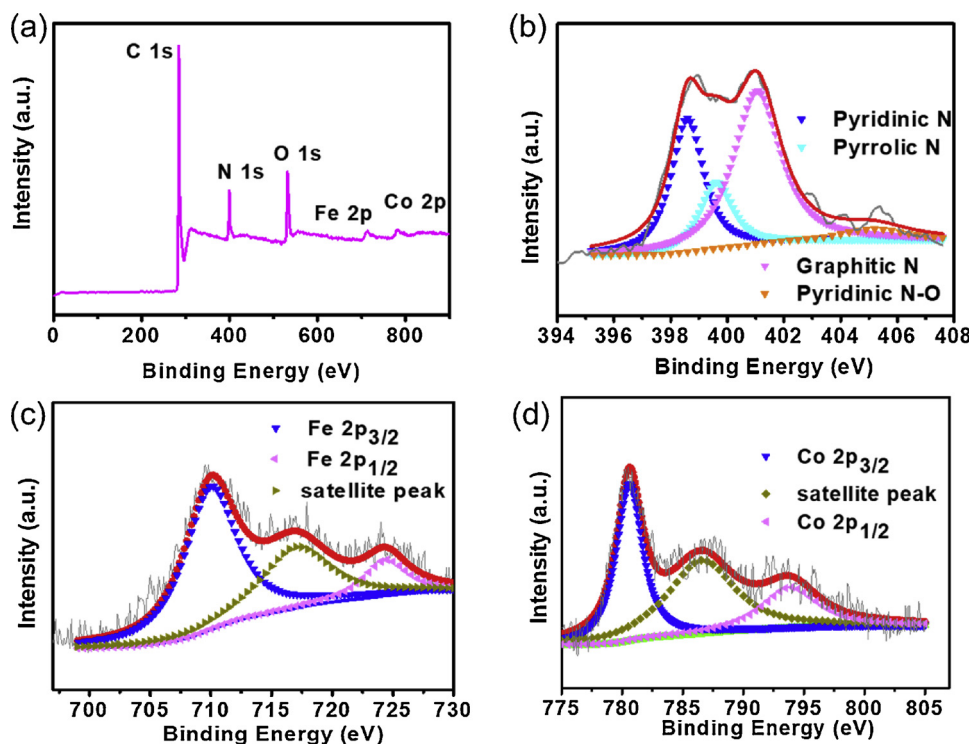


Fig. 4. (a) XPS survey spectra and high resolution of (b) N 1s (c) Fe 2p (d) Co 2p of FeCo@MNC.

smallest Tafel slope (66 mV dec^{-1}) compared to FeCo@NC (80 mV dec^{-1}) and NC (105 mV dec^{-1}), which even close to that of Pt/C (60 mV dec^{-1}). The durability of the FeCo@MNC for ORR was further evaluated (Fig. S4). The current density of FeCo@MNC showed a low decay (about 3% in 0.1 M KOH) after running for 20,000 s and in contrast, commercial Pt/C suffered from a 12% loss, revealing that FeCo@MNC had better stability compared to Pt/C. The ORR performance of FeCo@MNC was also better than other non-precious metal

ORR catalysts (Table S2).

The electrocatalytic activities of the prepared materials for OER were also evaluated. Polarization curves shown in Fig. 6a indicated that to reach the current density of 10 mA cm^{-2} , FeCo@MNC required to have an over potential of 240 mV, which was smaller than that of FeCo@NC (300 mV) and Pt/C (510 mV), while the current density of NC could not reach to 10 mA cm^{-2} even at the maximum potential. This over potential value was also smaller than that of many other

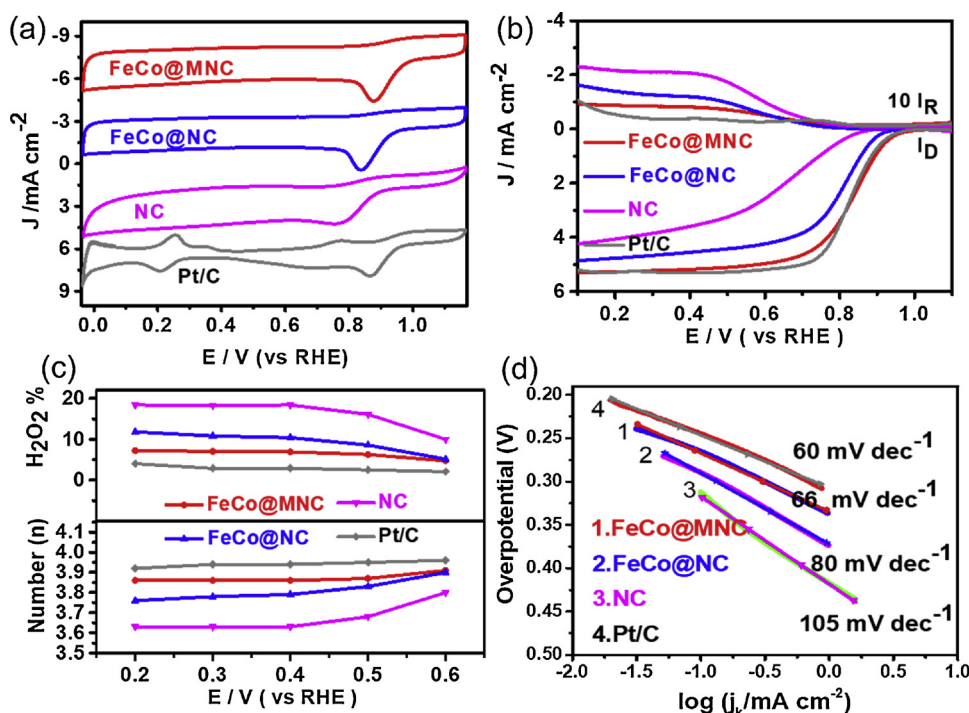


Fig. 5. (a) CV curves (b) RRDE polarization curves (c) the ORR electron transferred number and yield of H_2O_2^- (%) (d) Tafel slopes on NC, FeCo@NC, FeCo@MNC and Pt/C.

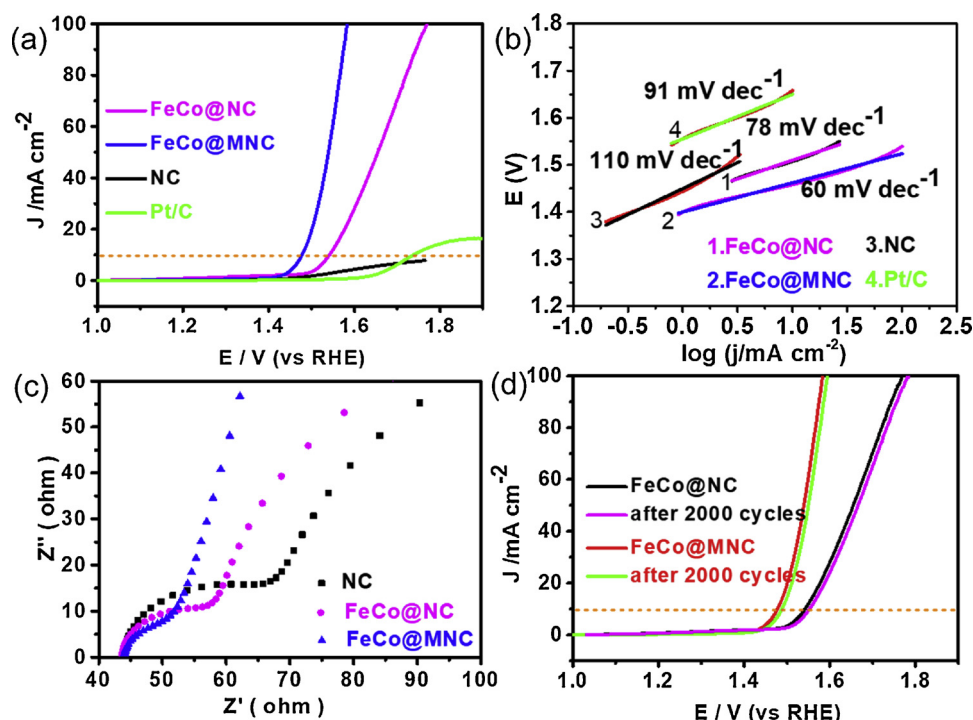


Fig. 6. (a) LSV polarization curves (b) The corresponding Tafel plots (c) Nyquist plots of NC, FeCo@NC, FeCo@MNC and Pt/C, respectively in OER process. (d) LSV polarization curves of FeCo@MNC before and after 2000 CV cycles.

reported OER electrocatalysts (Table S2). This excellent OER performance was further evidenced by the Tafel plots in Fig. 6b, showing that FeCo@MNC exhibited the lowest Tafel slope (60 mV dec^{-1}) for a fast kinetic process compared to FeCo@NC (78 mV dec^{-1}) and NC (110 mV dec^{-1}), and even lower than Pt/C (91 mV dec^{-1}). The excellent OER performance of FeCo@MNC should ascribe to the fast charge transfer, which could be estimated from impedance spectra (Fig. 6c) [41]. As illustrated in Fig. 6c, FeCo@MNC presented the lowest charge-transfer resistance in the high-frequency region, which was indicative of the fastest charge transfer process and suggested that Fe/Co/N co-doping was to greatly increase the electrical conductivity of the carbon nanofibers [42]. Besides, there was almost no decay in the LSV curves of FeCo@MNC after 2000 CV cycles, indicating a superior catalytic stability in the OER process.

3.3. Effect of chemical composition on ORR and OER activity

Two control samples, FeNC and CoNC nanofibers illustrated the existence of Fe-N and Co-N, respectively (Fig.S5, S6, and Table S1). As shown in Fig. 7a and b, the ORR and OER performance decreased in the following order: FeCo@MNC > FeNC, CoNC, which indicated that the co-existence of FeCo alloy and Fe/Co-N active sites could mostly promote the catalytic activity. To further evaluate the influence of amount of FeCo alloy on the performance of catalytic activity, FeCo@MNC-S with reduced FeCo alloy has been prepared (Fig.S7 and Table S1). Compared to FeCo@MNC, FeCo@MNC-S with fewer FeCo alloy exhibited lower catalytic activity (Fig.7), indicating that appropriate large amount of FeCo alloy would built up efficient bifunctional catalyst. However, FeCo@MNC with increased Fe and Co precursors during the electrospinning would lead to the failure of nanofiber formation due to the resulting low polymer concentration unfavorable for processing [43].

To further confirm the existence of M-N-C components, we performed RDE measurements to check the ORR activity of NC, FeNC, CoNC, and FeCo@MNC in 0.1 M KOH containing 0.01 M KCN (Fig. 7d). Cyanide (CN^-) as a probe ion to block the Fe-N (or Co-N) site has been

usually applied to justify the active site contains iron or cobalt [44,45]. Except NC, the half-wave potential of CoNC, FeNC, and FeCo@MNC was found to decrease significantly by 80, 95, and 110 mV, respectively, with the decrease of diffusion-limiting current. The decrease also suggested the formation of Fe-N-C and Co-N-C in the MNC samples..

The above experimental results suggested that FeCo@MNC was efficient towards the ORR and OER. Such outstanding catalytic performance of FeCo@MNC could be attributed to several factors. First of all, Co-existence of FeCo alloy and Fe/Co-N active sites could promote the catalytic activity of ORR and OER. Moreover, electrospinning based constrained-volume method ensured the precursors uniformly carbonized and dispersed within the carbon matrix after a pyrolysis process, efficiently avoiding the agglomeration of FeCo alloy nanoparticles. The above structural advantages also in a large part benefited from the use of PAN as a carbon precursor: 1) PAN provided the perfect filamentation for carbon nanofiber fabrication; 2) carbonized PAN nanofibers as one-dimensional carbon supporters for Fe, Co, N distribution, showed larger aspect ratio (lower diameter or larger length) and demonstrated excellent electrical conductivity. In addition, Fe/Co/N co-doping have greatly increased the electrical conductivity of the carbon nanofibers. Besides, the existence of numerous mesopores caused by PVP decomposition were beneficial for more active sites exposed to the reactants and rapid transportation of O_2 for ORR and OER.

3.4. Zn-air cell test

To comprehend the activity of the bifunctional catalyst, we further assessed its potential for practical application by assembling it into a primary Zn-air battery. As shown in Fig. 8a, a polished zinc plate was used as the metal anode and FeCo@MNC as the air cathode, with 0.2 M $\text{Zn}(\text{CH}_3\text{COO})_2$ added in 6 M KOH electrolyte to evaluate the discharge and charge performance of the battery respectively. The open-circuit potential of the Zn-air battery was 1.41 V (Fig. 8b). The discharge and charge polarization curves of FeCo@MNC and Pt/C were shown in Fig. 8c. FeCo@MNC showed a lower potential gap than that of Pt/C, indicating the better recharge ability of the former. The power density

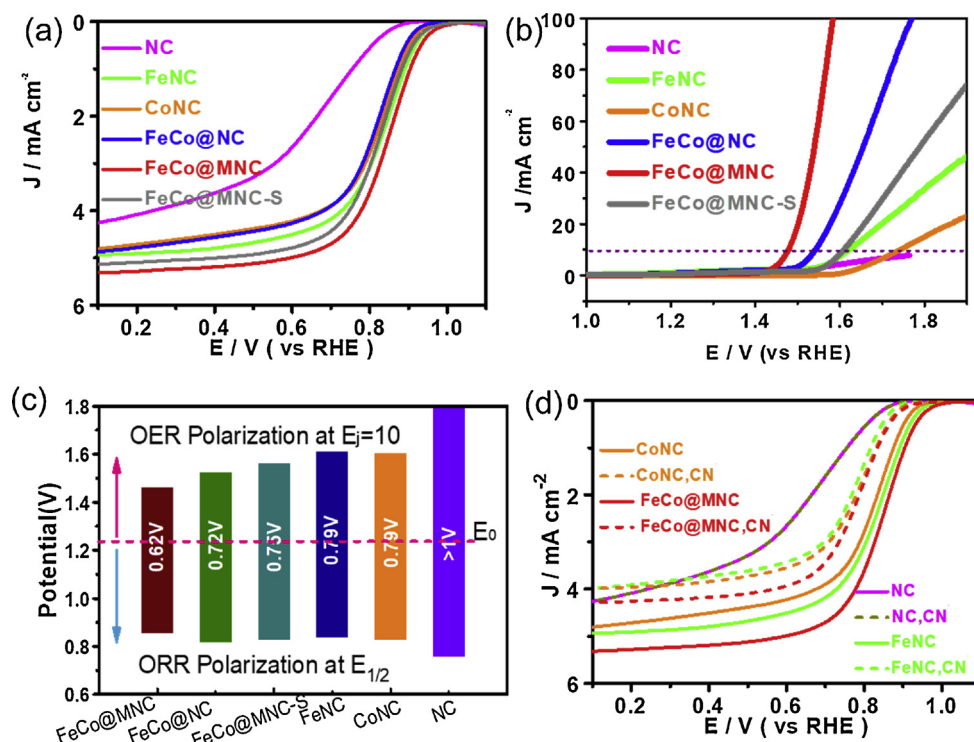


Fig. 7. LSV polarization curves of NC, FeNC, CoNC, FeCo@NC, FeCo@MNC, and FeCo@MNC-S in (a) ORR (b) OER process. (c) Overpotentials between the $E_{1/2}$ of ORR and $E_{j=10}$ of OER for all samples. (d) LSV polarization curves of NC, FeNC, CoNC, and FeCo@MNC before and after addition of 0.01 M KCN, respectively.

of the Zn-air battery catalyzed by FeCo@MNC in comparison with Pt/C were shown in Fig. 8d. The peak power density of FeCo@MNC at 143 mA cm^{-2} reached 115 mW cm^{-2} , 16 mW cm^{-2} higher than the power density of Pt/C (maximum 99 mW cm^{-2}). The performance and stability of FeCo@MNC and Pt/C was further investigated. The battery demonstrated excellent cycling stability at the constant current density of 20 mA cm^{-2} for 24 h with a 10 min cycling period. The charge-discharge voltage gap of FeCo@MNC (0.9 V, discharge-charge at 20 mA cm^{-2}) was lower than that of Pt/C (1.9 V, discharge-charge at 20 mA cm^{-2}), agreeing well with the polarization curves, which significantly resulted from the better recharge ability of the FeCo@MNC catalyst

(Fig. 8e). The excellent stability of FeCo@MNC also could be exemplified by continuous lighting of a light emitting diode (LED) pattern ($\sim 3 \text{ V}$) by two integrated Zn-air batteries in series for over 48 h without no obvious brightness decay (Fig. 8f and g).

4. Conclusion

In summary, we have synthesized mesoporous Fe/Co-N-C nanofibers with embedding FeCo nanoparticles (FeCo@MNC) via a facile and high-yield electrospinning method followed by a heat treatment in N_2 atmosphere. The materials exhibited a well-defined fibrous

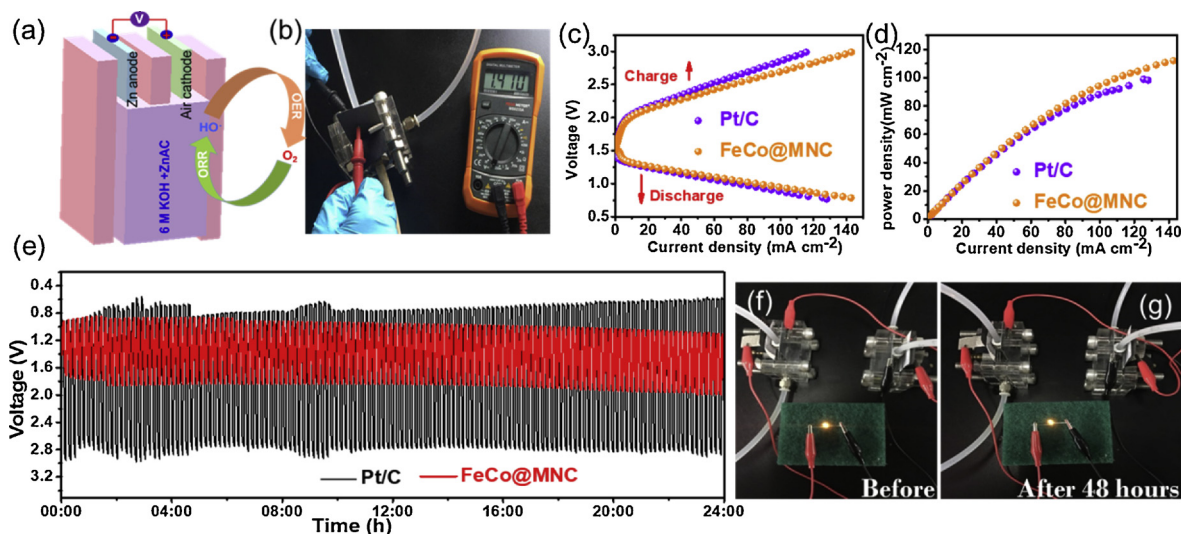


Fig. 8. (a) Scheme and (b) Open-circuit potential of the Zn – air battery. (c) Charge and discharge polarization curves and (d) power density of Zn – air batteries with FeCo@MNC and Pt/C. (e) Galvanostatic discharge-charge cycling curves at 20 mA cm^{-2} of rechargeable Zn – air batteries with FeCo@MNC and Pt/C catalyst on carbon paper, respectively. A lighted yellow LED ($\sim 3 \text{ V}$) powered by two integrated Zn – air batteries interconnected in series (f) before, and (g) after 48 h. (For interpretation of the references to colour in this figure legend, the reader is referred to the web version of this article.)

morphology, numerous mesoporous structure, uniformly distributed FeCo alloy nanoparticles and Fe/Co-N-C active sites. All these combined features eventually made FeCo@MNC an excellent bifunctional electrocatalyst toward ORR and OER. Furthermore, the catalyst outperformed Pt/C when served as an air cathode in a home-built liquid rechargeable Zn-air batteries. The approach may drive new insight to design other cost-efficient multifunctional catalysts for rechargeable Zn-air batteries.

Notes

The authors declare no competing financial interest.

Acknowledgements

We would like to acknowledge Shanghai Municipal Natural Science Foundation (No. 17ZR1432200), National Natural Science Foundation of China (No. 21774095), Fundamental Research Funds for the Central Universities (No. 0400219376), the start-up funding from Tongji University and the Young Thousand Talented Program.

Appendix A. Supplementary data

Supplementary material related to this article can be found, in the online version, at doi:<https://doi.org/10.1016/j.apcatb.2018.11.039>.

References

- [1] J. Yin, Y. Li, F. Lv, M. Lu, K. Sun, W. Wang, L. Wang, F. Cheng, Y. Li, P. Xi, S. Guo, Oxygen vacancies dominated NiS₂/CoS₂ interface porous nanowires for portable Zn-Air batteries driven water splitting devices, *Adv. Mater.* 29 (2017) 1704681.
- [2] P. Tan, B. Chen, H. Xu, W. Cai, W. He, M. Ni, In-situ growth of Co₃O₄ nanowire-assembled clusters on nickel foam for aqueous rechargeable Zn-Co₃O₄ and Zn-air batteries, *Appl. Catal. B: Environ.* 241 (2019) 104–112.
- [3] Z. Pei, H. Li, Y. Huang, Q. Xue, Y. Huang, M. Zhu, Z. Wang, C. Zhi, Texturing in situ: N,S-enriched hierarchically porous carbon as a highly active reversible oxygen electrocatalyst, *Energ. Environ. Sci.* 10 (2017) 742–749.
- [4] X. Zheng, J. Wu, X. Cao, J. Abbott, C. Jin, H. Wang, P. Strasser, R. Yang, X. Chen, G. Wu, N. P., and S-doped graphene-like carbon catalysts derived from Onium Salts with enhanced oxygen chemisorption for Zn-air battery cathodes, *Appl. Catal. B: Environ.* 241 (2018) 442–451.
- [5] K. Gong, F. Du, Z. Xia, M. Durstock, L.M. Dai, Nitrogen-doped carbon nanotube arrays with high electrocatalytic activity for oxygen reduction, *Science* 323 (2009) 760–764.
- [6] J. Ying, G. Jiang, Z.P. Cano, Z. Ma, C. Zhong, D. Su, Z. Chen, Metal-organic frameworks derived platinum-cobalt bimetallic nanoparticles in nitrogen-doped hollow porous carbon capsules as a highly active and durable catalyst for oxygen reduction reaction, *Appl. Catal. B: Environ.* 225 (2018) 496–503.
- [7] J. Choi, J.H. Jang, C.W. Roh, S. Yang, J. Kim, J. Lim, H. Lee, Gram-scale synthesis of highly active and durable octahedral PtNi nanoparticle catalysts for proton exchange membrane fuel cell, *Appl. Catal. B: Environ.* 225 (2018) 530–537.
- [8] G.F. Chen, T.Y. Ma, Z.Q. Liu, N. Li, Y.Z. Su, K. Davey, S.Z. Qiao, Efficient and stable bifunctional electrocatalysts Ni/Ni_xM_y (M = P, S) for overall water splitting, *Adv. Funct. Mater.* 26 (2016) 3314–3323.
- [9] J.X. Feng, H. Xu, Y.T. Dong, S.H. Ye, Y.X. Tong, G.R. Li, FeOOH/Co/FeOOH Hybrid Nanotube Arrays as High-Performance Electrocatalysts for the Oxygen Evolution Reaction, *Angew. Chem.* 55 (2016) 3694–3698.
- [10] J.X. Feng, S.H. Ye, H. Xu, Y.X. Tong, G.R. Li, Design and synthesis of FeOOH/CeO₂ heterolayered nanotube electrocatalysts for the oxygen evolution reaction, *Adv. Mater.* 28 (2016) 4698–4703.
- [11] Y. Mun, M.J. Kim, S.A. Park, E. Lee, Y. Ye, S. Lee, Y.E. Sung, Soft-template synthesis of mesoporous non-precious metal catalyst with Fe-Nx/C active sites for oxygen reduction reaction in fuel cells, *Appl. Catal. B: Environ.* 222 (2018) 191–199.
- [12] L. Partanen, G. Mordachaw, K.E. Laasonen, Oxygen evolution reaction kinetic barriers on nitrogen-doped carbon nanotubes, *J. Phys. Chem. C* 122 (2018) 12892–12899.
- [13] G. Anandhababu, S.C. Abbas, J. Lv, K. Ding, Q. Liu, D.D. Babu, Y. Wang, Highly exposed Fe-N₄ active sites in porous poly-iron-phthalocyanine based oxygen reduction electrocatalyst with ultrahigh performance for air cathode, *Dalton Trans.* 46 (2017) 1803–1810.
- [14] G. Fu, Z. Cui, Y. Chen, Y. Li, Y.X. Lin, J.B. Tang, Goodenough, Hierarchically mesoporous nickel-iron nitride as a cost-efficient and highly durable electrocatalyst for Zn-air battery, *Nano Energy* 39 (2017) 77–85.
- [15] W. Ahn, M.G. Park, D.U. Lee, M.H. Seo, G. Jiang, Z.P. Cano, F.M. Hassan, Z.W. Chen, Hollow multivoid nanocuboids derived from ternary Ni-Co-Fe prussian blue analog for dual-electrocatalysis of oxygen and hydrogen evolution reactions, *Adv. Funct. Mater.* 28 (2018) 1802129.
- [16] Y. Yang, L. Zhuang, R. Lin, M. Li, X. Xu, T.E. Rufford, Z. Zhu, A facile method to synthesize boron-doped Ni/Fe alloy nano-chains as electrocatalyst for water oxidation, *J. Power Sources* 349 (2017) 68–74.
- [17] Y. Fu, H.Y. Yu, C. Jiang, T.H. Zhang, R. Zhan, X. Li, J.F. Li, J.H. Tian, R.Z. Yang, A facile method to synthesize boron-doped Ni/Fe alloy nano-chains as electrocatalyst for water oxidation, *Adv. Funct. Mater.* 28 (2018) 1705094.
- [18] X.F. Lu, L.F. Gu, J.W. Wang, J.X. Wu, P.Q. Liao, G.R. Li, Bimetal-organic framework derived CoFe₂O₄/C porous hybrid nanorod arrays as high-performance electrocatalysts for oxygen evolution reaction, *Adv. Mater.* 29 (2017) 1604437.
- [19] P. Cai, S. Ci, E. Zhang, P. Shao, C. Cao, Z. Wen, FeCo alloy nanoparticles confined in carbon layers as high-activity and robust cathode catalyst for Zn-air battery, *Electro. Acta* 220 (2016) 354–362.
- [20] N. Wu, Y. Lei, Q. Wang, B. Wang, C. Han, Y. Wang, Facile synthesis of FeCo@ NC core-shell nanospheres supported on graphene as an efficient bifunctional oxygen electrocatalyst, *Nano Res.* 10 (2017) 2332–2343.
- [21] Q. Liu, S. Cao, Y. Qiu, L. Zhao, Bimetallic Fe-Co promoting one-step growth of hierarchical nitrogen-doped carbon nanotubes/nanofibers for highly efficient oxygen reduction reaction, *Mater. Sci. Eng.* 223 (2017) 159–166.
- [22] S. Sultan, J.N. Tiwari, J.-H. Jang, A.M. Harzandi, F. Salehnia, S.J. Yoo, K.S. Kim, Highly efficient oxygen reduction reaction activity of graphitic tube encapsulating nitrated Co₉Fe₇ alloy, *Adv. Energy Mater.* (2018) 1801002.
- [23] N. Wu, Y. Wang, Y. Lei, B. Wang, C. Han, Y. Gou, Q. Shi, D. Fang, Electrospun interconnected Fe-N/C nanofiber networks as efficient electrocatalysts for oxygen reduction reaction in acidic media, *Sci. Rep.* 5 (2015) 17396.
- [24] Q. Liu, Y. Wang, L. Dai, J. Yao, Scalable fabrication of nanoporous carbon fiber films as bifunctional catalytic electrodes for flexible Zn-air batteries, *Adv. Mater.* 28 (2016) 3000–3006.
- [25] Y. Lu, S. Du, R. Steinberger-Wilkens, One-dimensional nanostructured electrocatalysts for polymer electrolyte membrane fuel cells-a review, *Appl. Catal. B: Environ.* 199 (2016) 292–314.
- [26] J.E. Park, M.J. Kim, M.S. Lim, S.Y. Kang, J.K. Kim, S.H. Oh, M. Her, Y.H. Cho, Y.E. Sung, Graphitic carbon nitride-carbon nanofiber as oxygen catalyst in anion-exchange membrane water electrolyzer and rechargeable metal-air cells, *Appl. Catal. B: Environ.* 237 (2018) 140–148.
- [27] J.X. Feng, H. Xu, S.H. Ye, G. Ouyang, Y.X. Tong, G.R. Li, In situ formed Fe-N doped metal organic framework@ carbon nanotubes/graphene hybrids for a rechargeable Zn-air battery, *Angew. Chem. Int. Ed.* 56 (2017) 8120–8124.
- [28] C. Li, J. Zhao, R.D. Priestley, R. Liu, Constrained-volume assembly of organometal confined in polymer to fabricate multi-heteroatom doped carbon for oxygen reduction reaction, *Sci. China Mater.* (2018) 1–9.
- [29] Z.Y. Chen, Q.C. Wang, X.B. Zhang, Y.P. Lei, W. Hu, Y. Luo, Y.B. Wang, N-doped defective carbon with trace Co for efficient rechargeable liquid electrolyte/all-solid-state Zn-air batteries, *Sci. Bull. (Beijing)* 63 (2018) 548–555.
- [30] H. Yu, Q. Zhang, M. Dahl, J.B. Joo, X. Wang, L. Wang, Y. Yin, Dual-pore carbon shells for efficient removal of humic acid from water, *Chem. Eur. J.* 23 (2017) 16249–16256.
- [31] Z. Qiang, J. Xue, K.A. Cavicchi, B.D. Vogt, Morphology control in mesoporous carbon films using solvent vapor annealing, *Langmuir* 29 (2013) 3428–3438.
- [32] Z.C. Chen, X.M. Gao, X.R. Wei, X.X. Wang, Y.G. Li, T. Wu, J. Guo, Q. Gu, W.D. Wu, X.D. Chen, Z. Wu, D.Y. Zhao, Directly anchoring Fe₃C nanoclusters and FeN₄ sites in ordered mesoporous nitrogen-doped graphitic carbons to boost electrocatalytic oxygen reduction, *Carbon* 121 (2017) 143–153.
- [33] G. Wang, B.Q. Qian, Y.W. Wang, Q. Dong, F. Zhan, J.S. Qiu, Electrospun porous hierarchical carbon nanofibers with tailored structures for supercapacitors and capacitive deionization, *New J. Chem.* 40 (2016) 3786–3792.
- [34] W.G. Wang, D.D. Babu, Y.Y. Huang, J.Q. Lv, Y.B. Wang, M.X. Wu, Atomic dispersion of Fe/Co/N on graphene by ball-milling for efficient oxygen evolution reaction, *Int. J. Hydrogen Energy* 43 (2018) 10351–10358.
- [35] Q.P. Lin, X.H. Bu, A.G. Kong, C.Y. Mao, X. Zhao, F. Bu, P.Y. Feng, New heterometallic zirconium metalloporphyrin frameworks and their heteroatom-activated high-surface-area carbon derivatives, *J. Am. Chem. Soc.* 137 (2015) 2235–2238.
- [36] T. Palaniselvam, V. Kashyap, S.N. Bhang, J.B. Baek, S. Kurungot, Nanoporous graphene enriched with Fe/Co-N active sites as a promising oxygen reduction electrocatalyst for anion exchange membrane fuel cells, *Adv. Funct. Mater.* 26 (2016) 2150–2162.
- [37] L. Zeng, X.Z. Cui, L. Chen, T. Ye, W. Huang, R.G. Ma, J. Shi, Non-noble bimetallic alloy encased in nitrogen-doped nanotubes as a highly active and durable electrocatalyst for oxygen reduction reaction, *Carbon* 114 (2017) 347–355.
- [38] X. Zhu, T. Jin, C.C. Tian, C.B. Lu, X.M. Liu, M. Zeng, X.D. Zhuang, S.Z. Yang, L. He, H.L. Liu, S. Dai, In situ coupling strategy for the preparation of FeCo alloys and co4n hybrid for highly efficient oxygen evolution, *Adv. Mater.* 29 (2017) 1704091.
- [39] L. Jiao, G. Wan, R. Zhang, H. Zhou, S.H. Yu, H.L. Jiang, From Metal-organic frameworks to single-atom Fe implanted n-doped porous carbons: efficient oxygen reduction in both alkaline and acidic media, *Angew. Chem. Int. Ed.* 57 (2018) 8525–8529.
- [40] A.G. Kong, Y.Y. Kong, X.F. Zhu, Z. Han, Y.K. Shan, Ordered mesoporous Fe (or Co)-N-graphitic carbons as excellent non-precious-metal electrocatalysts for oxygen reduction, *Carbon* 78 (2014) 49–59.
- [41] L. Kavan, H. Krysova, P. Janda, H. Tarabkova, Y. Saygili, M. Freitag, S.M. Zakeeruddin, A. Hagfeldt, M. Grätzel, Novel highly active Pt/graphene catalyst for cathodes of Cu (II/I)-mediated dye-sensitized solar cells, *Electrochem. Acta* 251 (2017) 167–175.
- [42] Z.W. Hu, Z.Y. Guo, Z.P. Zhang, M. Dou, F. Wang, Bimetal zeolitic imidazolate framework-derived iron-, cobalt-and nitrogen-codoped carbon nanopolyhedra electrocatalyst for efficient oxygen reduction, *ACS Appl. Mater. Interfaces* 10 (2018) 12651–12658.

- [43] C. Mit-uppatham, M. Nithitanakul, P. Supaphol, Ultrafine electrospun polyamide-6 fibers: effect of solution conditions on morphology and average fiber diameter, *Macromol. Chem. Phys.* 205 (2004) 2327–2338.
- [44] Q. Wang, Z.Y. Zhou, Y.J. Lai, Y. You, J.G. Liu, X.L. Wu, E. Terefe, C. Chen, L. Song, M. Rauf, N. Tian, Phenylenediamine-based FeN x/C catalyst with high activity for oxygen reduction in acid medium and its active-site probing, *J. Am. Chem. Soc.* 136 (2014) 10882–10885.
- [45] M. Zeng, Y. Liu, F. Zhao, K. Nie, N. Han, X. Wang, W. Huang, X. Song, J. Zhong, Y. Li, Metallic cobalt nanoparticles encapsulated in nitrogen-enriched graphene shells: its bifunctional electrocatalysis and application in zinc–air batteries, *Adv. Funct. Mater.* 26 (2016) 4397–4404.